

INFLUENCE OF HEAT IN THE MICROSTRUCTURE OF AISI 301 STAINLESS STEEL CAST ZONE AISI 301

¹Wandercleiton Cardoso

²Thiago Augusto Pires Machado*

³Raphael Colombo Baptista

⁴André Gustavo de Souza Galdino

⁵Flavio Antonio de Moraes Pinto

⁶Temistocles de Sousa Luz

¹Università degli Studi di Genova: wandercleiton.cardoso@dicca.unige.it

²Instituto Federal do Espírito Santo: thiagoaugustopn@yahoo.com.br

³Instituto Federal do Espírito Santo: colombo.rafael@hotmail.com

⁴Instituto Federal do Espírito Santo: andregsg@ifes.edu.br

⁵Instituto Federal do Espírito Santo: flaviop@ifes.edu.br

⁶Universidade Federal do Espírito Santo: temistocles.luz@ufes.br

*Corresponding author

Article submitted on 05/17/2021, accepted on 10/08/2021 and published on 11/19/2021.

Abstract: The aim of this work was to evaluate the effects of the variation of welding energy on the microstructure and mechanical properties of the fusion zone of AISI 301 stainless steel, to quantify the delta ferrite phase and to observe the effects of this phase on the fusion zone of the weld bead. Semi-Automatic Granulometer (GSA) software was used to quantify the delta ferrite. Five samples were prepared, each with different welding parameters. The welding method selected was autogenous tungsten inert gas (TIG). The results confirmed that the welding energy has a great influence on the amount of delta ferrite formed in the molten zone of the weld bead, and the decrease of delta ferrite amount was also confirmed with the increase of welding energy.

Keywords: AISI 301 stainless steel, TIG welding, welding energy.

1 INTRODUCTION

The extraction and processing of iron and steel has undergone continuous technical progress throughout nearly 5,000 years of history. Despite the great efforts of metallurgists, some problems remained unsolved until the beginning of the last century: objects made of iron and steel were not sufficiently resistant to corrosion (KUDDUS, 2018).

In 1911, in the United States of America, experiments with alloys containing 14-16%Cr and 0.007-0.015%C led to the discovery of ferritic stainless steels, which are still used today by designers for the manufacture of turbines.

In 1912, researchers in England conducted experiments with corrosion-resistant alloys containing 12.8%Cr and 0.24%C, leading to the discovery of martensitic stainless steels. In the same

year, a steel containing 7%Ni, 20%Cr and 0.25%C was produced in Germany for the manufacture of parts that required high corrosion resistance, giving rise to austenitic stainless steels (GIRALDO, 2011).

Austenitic stainless steels are the most produced and marketed in the world. Between 1950 and 1980, the production of stainless steels increased 20-fold and currently austenitic stainless steels account for 2/3 of this production (RISHNAN *et al.*, 2021).

This wide use is due to an advantageous combination of properties, such as: excellent corrosion and oxidation resistance, mechanical strength at high temperatures, excellent ductility and weldability (CARDOSO, 2012; CASALINO *et al.*, 2018).

However, it should be taken into account that most metals, including austenitic stainless steels, undergo several microstructural changes during the welding process, in particular intergranular corrosion (sensitization) characterized by the formation of chromium carbides in the contours of the grain. The formation of these carbides leaves chromium-depleted areas near the grain boundaries that are susceptible to this type of deterioration (RISHNAN *et al.*, 2021; GENG *et al.*, 2019; BALRAM *et al.*, 2019a).

Welding of stainless steels must be done very carefully to maintain the mechanical properties and corrosion resistance of the welded area (AVINASH *et al.*, 2019; HAN *et al.*, 2019; BALRAM *et al.*, 2019b).

Numerous researchers have observed the effects of welding on the microstructure and properties of the welded area, so we have a wide range of information on this topic (CHENITI *et al.*, 2019; MOHARANA *et al.*, 2020; SHANM *et al.*, 2020; MISHRA and DAKKILI, 2020).

It is well known that the environment of the welded area and even the molten area undergo microstructural changes due to a variety of thermal cycles resulting from a welding process (ARANTES, 2004; PERALTA, 2003; ZUMELZU and CABEZAS, 2021; CASALINO *et al.*, 2018).

Studies show that welding effects cause microstructural disturbances in the metal. To minimize such effects, austenite stabilizing elements can be added, either by shielding gas enriched with N or by post-weld heat treatment or by using nickel (Ni) enriched filler metal (LORA, 2006; ASADI *et al.*, 2020; SAROJ *et al.*, 2017; SOLTANI and TAYEBI, 2018; CORRÊA, 2012; SUN *et al.*, 2017; KUMAR *et al.*, 2021c).

The main problem in welding stainless steels is the possibility of transformation of the microstructure, which can occur through hardening by secondary precipitation of carbides or formation of intermetallic phases such as the sigma phase. In this case, the ductility of the material decreases and cracking during welding is almost inevitable (ITMAN *et al.*, 2013).

The aim of this paper is to evaluate the effects of welding energy on the microstructural changes in the molten area by quantifying delta ferrite and observing its effects on the area in order to minimize the effects of welding on the properties of AISI 301 stainless steel, thus reducing costs and problems for the industry.

2 CONTEXTUALIZATION

Stainless steels are corrosion resistant metal alloys containing at least 10.5% chromium, nickel, molybdenum and other additives such as niobium (CARDOSO, 2012; KUDDUS *et al.*, 2018).

While structural and engineering carbon steels meet the requirements for mechanical strength, weldability and toughness, there is a wide variety of

stainless steels suitable for environments where corrosion and mechanical resistance are critical requirements (TANG *et al.*, 2020).

Stainless steels are the result of the controlled addition of alloying elements that result in specific properties related to mechanical strength and corrosion resistance, especially in media with high chloride content (JIJIN *et al.*, 2017).

Stainless steels are classified into five basic families: ferritic, austenitic, martensitic, duplex and precipitation hardening (CARDOSO, 2012; KUDDUS *et al.*, 2018).

2.1 Ferritic stainless steels.

Ferritic stainless steels have a body centered cubic (CCC), are magnetic, less expensive compared to austenitic steels and have limited corrosion resistance (CARDOSO, 2012).

The main alloying element is chromium, with typical contents between 11-17% and a low carbon content, which results in these steels having limited mechanical strength compared to stainless steels of other classes (CARDOSO, 2012).

This class of stainless steels is not hardenable by heat treatment and generally has a yield strength of 275-350 MPa in the annealed condition (PANKAJ *et al.*, 2019).

Ferritic steels cost less than austenitic steels but have limited corrosion resistance compared to the more commonly used austenitic steels (CARDOSO, 2012; XIAOGANG *et al.*, 2018).

Ferritic steels are also limited in toughness, weldability, corrosion resistance, and formability compared to austenitic, martensitic, duplex, and precipitation hardening stainless steels, but they have some special applications, such as solenoid valve cores (CARDOSO, 2012; SHUANG *et al.*, 2017). Examples of

ferritic stainless steels: AISI 405, 430, 441, 436 and AISI 446.

2.2 Austenitic stainless steels

Austenitic stainless steels are the largest family in terms of number of alloys and uses. Since ferritic stainless steels are not hardenable by heat treatment, they have limited carbon content but contain nobler additives, mainly nickel, which is responsible for changing the microstructure to the face-centered cubic (CFC) configuration at room temperature, i.e. they are non-magnetic (CARDOSO, 2012; XIAOGANG *et al.*, 2018).

Austenitic stainless steels can be hardened by work hardening, which is accompanied by partial changes in the microstructure (CARDOSO, 2012; KANT *et al.*, 2018).

The most commonly used austenitic stainless steels are types 301 and 304, which contain more than 16% chromium and 6% nickel and are characterized by excellent ductility, formability and toughness, even at cryogenic temperatures (MARUTHI *et al.*, 2018).

Molybdenum is an alloying element added to some austenitic steels to increase resistance to localized corrosion mechanisms such as galvanic, pitting and alveolar corrosion (CARDOSO, 2012).

According to Kejelin (2019), austenitic stainless steels are prone to hot cracking, especially when welded and using wear parts that resemble the structure of the base metal. Cracking, in turn, is caused by impurities that are difficult to dissolve, have a lower melting point and are located in the grain boundaries of the austenitic structure.

It is worth noting that cracking occurs in the molten zone and/or in the thermally affected zone. In general, such steels dissolve hydrogen well and do not harden during cooling. For this reason, they are not susceptible to cold cracking. However, there are problems that are not

noticed during welding, such as loss of mechanical properties, resistance to heat, wear and corrosion (KEJELIN *et al.*, 2019).

It is known that the property of corrosion resistance is related to the formation of a passivating (protective) film of chromium oxide, which ensures the stainless properties of the steel (ITMAN *et al.*, 2013; ITMAN *et al.*, 2014).

When transformation takes place in the range that leads to a decrease in chromium content (%) in the solid solution, it in turn becomes susceptible to corrosion. This phenomenon, which occurs between 400 and 800°C, is called sensitization and results from the combination of elements that have an affinity for chromium, such as carbon and nitrogen, which form carbides and nitrides, respectively (KRIPALANI *et al.*, 2021; KUMAR *et al.*, 2019).

According to Kejelin (2019), to reduce this type of corrosion, it is recommended to use welding processes with low heat input, without preheating and with cold treatment.

Another problem related to reduced corrosion resistance is the corrosive process called prefer.

3 MATERIALS AND METHODS

The samples were first dissolved at 1100°C. The technique of optical emission spectrometry (Oxford Instruments, Foundry-Master model) with argon plasma was used to determine the chemical composition, which is widely used in environmental analysis because it has a number of features, such as multi-element analysis, which allows the simultaneous determination of minor and trace metals, and low susceptibility to interference between elements. **Table 1** shows the chemical composition of the steel studied:

Table 1: Chemical composition of steel

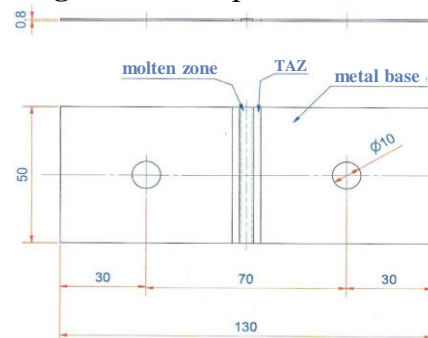
Component	Steel analyzed	Standard AISI 301
Cr	16,7%	16-18%
Ni	6,9%	6-8%
C	0,05%	<0.15%
Mn	1,8%	<2%
P	0,031%	<0.045%
Si	0,66%	<1%
S	0,001%	<0.030%
Mo	0,19%	-
Cu	0,13%	-
Nb	0,02%	-

Source: Prepared by the authors.

The specimens were prepared in the form of 0.8 mm thick and 50 mm wide laminated sheets, according to the schematic drawing of the **Figure 1**.

The specimen is not standardized, but Annex B of the NBR 10663 standard (ABNT, 2016) was used as a reference for the fabrication.

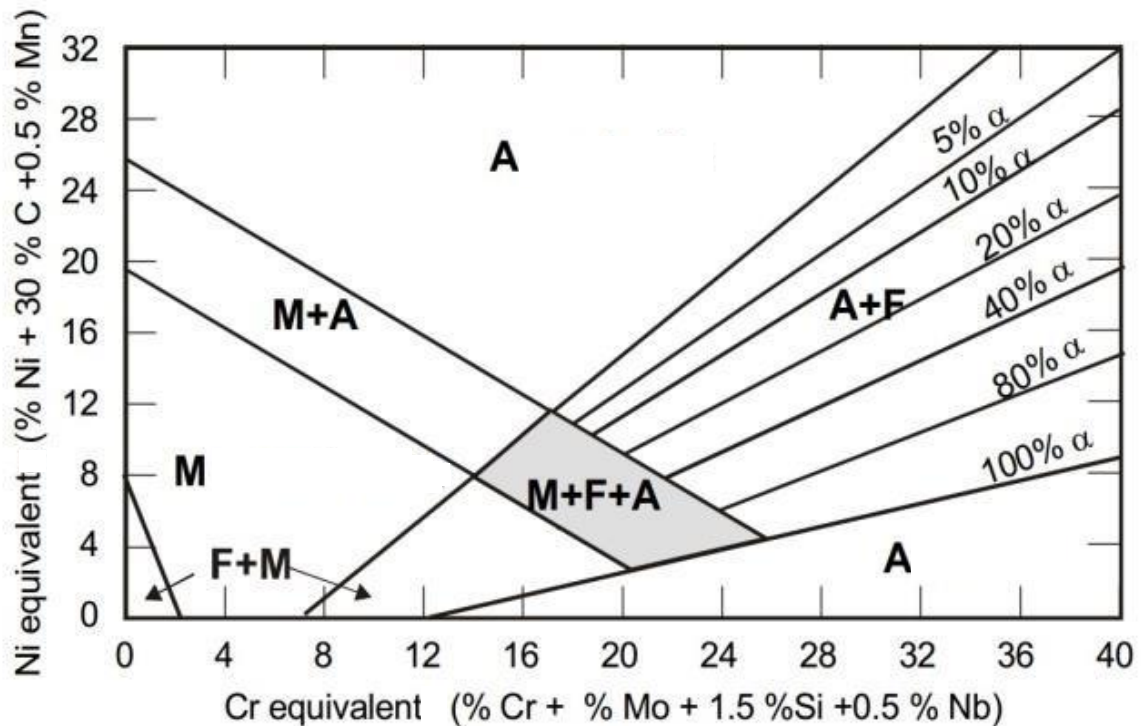
Figure 1: Test specimen sketch



Source: Prepared by the authors.

The C_{req}/N_{ieq} ratio was calculated based on the chemical analysis of AISI 301, as shown in **Figure 2**, to verify if the formation of ferrite is favored as the first stage of solidification and during this process the formation of austenite occurs, resulting in a double structure (austenite and ferrite) in the solid state (KANT *et al.*, 2018).

Figure 2: Schaeffler diagram



Source: Kejelin *et al.*, 2019

Regarding the welding methodology, the autogenous technique with one pass TIG was used because it allows a better control of the welding parameters and also produces a weld with a better surface (KRIPALANI and JAIN, 2021).

The displacement along the width of the plate was automatic and the welding was performed with forward polarity (CC), in the flat position.

In order to proceed with the welding process, the plates were positioned so that they were well leveled to avoid variations in the distance between the electrode and the part, thus maintaining a constant welding voltage across the width of the plate.

Five specimens were made using the Inverse 450 as power source, belonging to the Welding Laboratory of the

Technological Center of the Federal University of Espírito Santo (UFES).

For each of the 5 samples, different drilling parameters were established in order to analyze the influence of the welding energy imposed on the final microstructure and the characteristics of the fusion zone of the metal due to the variation of the heat introduced in the systems.

The parameters for each sample are listed in **Table 2**, as well as the welding energy calculated using **Equation (1)**.

Table 2: Parameters used for welding specimens

Parameters	S1	S2	S3	S4	S5
Current (A)	24.0	22.0	24.0	25.0	22.0
Voltage (V)	9.8	9.3	10.4	9.2	9.7
Welding speed (cm/min)	15.0	9.0	13.0	9.0	9.0
Gas flow (l/min)	10.0	10.0	10.0	10.0	10.0
Welding energy (kJ/cm)	0.94	1.12	1.16	1.53	1.42

Source: Prepared by the authors.

$$E = \frac{U \cdot I}{v} \quad (1)$$

Where the energy (E) is expressed in kJ/cm the welding voltage (U) in volts, the welding current (I) in amperes (A), and the welding speed (ws) in cm/min. (KEJELIN et al., 2019)

In order to visualize the differences resulting from the different energies acting on the microstructure and properties of the molten zone, a metallographic analysis and later a quantification of the micro constituents (delta ferrite) were performed using Semi-Automatic Granulometer (GSA) software.

Pure argon was used as the shielding gas with a flow rate of 10 l/min. An angle of 60° and a distance of 3.0 mm were partially maintained at the tip of the tungsten electrode doped with 2% thorium.

In order to reduce the bulging of the plates and to obtain a more stable weld bead, a small fixture was made to fix the specimens, as shown in **Figure 3**.

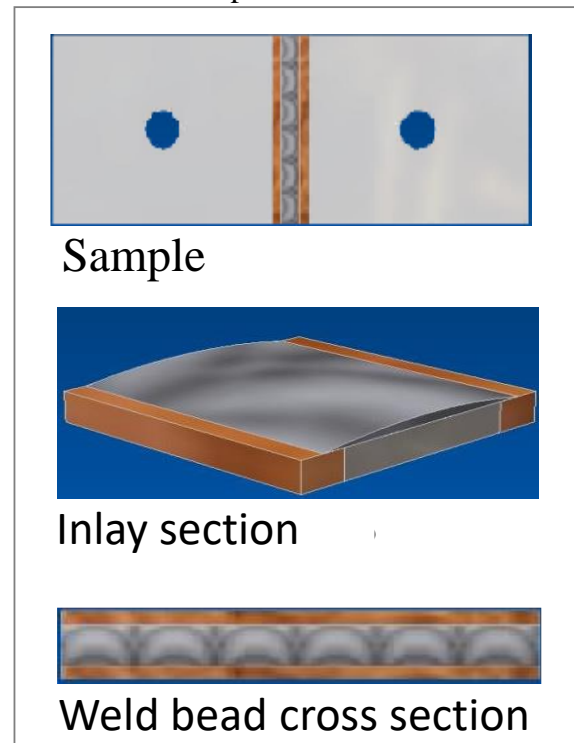
Figure 3: Specimen support



Source: Prepared by the authors.

The welded specimens were subjected to a cross section of the weld bead, using the fusion line as a reference. For each insert, a cross-section was made according to the schematic drawings in **Figure 4**.

Figure 4: Procedure for welding the specimens.



Source: Prepared by the authors.

Specimens were cut using a guillotine from the Mechanical Technology Laboratory at UFES. First, the cuts were made parallel to the weld bead to capture the melted zone and the thermally affected zone of the bead.

Shortly after, a small section of the sample in question was removed to obtain a cut for metallographic analysis. After removing the sections, they were embedded with a thermosetting hot curing resin (Bakelite) to facilitate handling.

Then the specimens were sanded, first with 320 grit sandpaper, then with 400, 600, 1000 and finally with 1200. With each successive sandpaper, the direction was changed by 90° until the traces of the previous sandpaper had disappeared. Polishing of the specimens was done manually with a polishing cloth moistened with the alumina polishing agent. The

samples were first pre-polished with 1 μ alumina to reduce the thickness of the deformed layer, and then final polished with 0.3 μ alumina to remove scratches from the sample surface.

A mixture of 15 ml hydrochloric acid (HCl), 10 ml nitric acid (HNO₃) and 10 ml acetic acid was used to chemically etch the stainless steel. The chemical attack was carried out by immersing the part in the reagent for 10 seconds. It was then sealed under running water and dried by soaking in ethyl alcohol.

After chemical attack, the samples were examined under optical microscope. Metalux-3-Leitz optical microscope was used to evaluate the melted zone. For each sample 5 (five) different microscopic images of the molten area of the cord were taken, for a total of 25 samples, with a 500x magnification scale.

Quantitative computed image metallography is a relatively new field in metallurgy, which explains the lack of technical training for most professionals. Despite the large number of publications on the subject, most focus on the development and comparison of methods rather than their practical application and processing in software.

For quantification of delta ferrite at work, GSA, a computerized system for grain size calculation and quantification, was used. In order to determine the volume fraction, the GSA software was based on linear analysis as this is the most commonly used method for calculating grain size and provides an interface where interaction with the user is great. Of the three forms of analysis that use two-dimensional planes (area analysis, linear analysis, and point counting), linear analysis is less accurate.

However, in procedures that require many measurements and in the analysis of

very fine structures, this method proves to be quite applicable. The marked lines were stored in a matrix with 4 columns, and the coordinates of the start and end points of the marking were already correctly fitted to the grid by the program. These data provided the average length of the lines, i.e. the arithmetic mean of the total distances.

From the information in the matrix and the compilation of a histogram, where the number of areas is defined as the square root of n , where n is the number of marks made by the user, the variance and standard deviation were also calculated. In order to calculate the set of microcomponents, a simple arithmetic calculation was used to determine the percentage of line lengths that hit the surfaces of the microcomponents. The GSA software is a line intersection system used to quantify the microcomponents present in the imaged region.

A magnification of 500x with a resolution of 100 dpi was used. The mesh generated for quantification of delta ferrite consisted of 4 vertical and 4 horizontal lines. As described previously, the percent quantification of delta ferrite for each of the 5 samples was performed using the percent average of the values obtained from the quantification of the photomicrographs of each sample (25 photos in total).

4 RESULTS AND DISCUSSION

Faster than expected cooling was observed in the fabrication of the specimens, assuming three-dimensional heat flow, which is characteristic of thicker sheets. For thinner sheets, the part cools more slowly (KUMAR, 2021b).

Based on the observations made during the welding of the parts and the analysis of the observations on the variation of the cooling rate as a function

of the thickness of the fabricated sheet, it is believed that the backing used to fix the specimens influenced the increase in the heat flux, due to the increase in the mass present in the system, which facilitated the heat flux by conduction and caused a significant increase in the cooling rate (KUMAR *et al.*, 2019; GNANASEKARAN *et al.*, 2021).

The authors Kumar *et al.* (2019) and Gnanasekaran *et al.* (2021) also emphasize the importance of the cooling rate parameter in determining the microstructure of the steel, which even affects the amount of ferrite remaining in the casting zone of welded parts.

Literature indicates that at high cooling rate, as considered in this study, the transformation of ferrite to austenite could be suppressed, resulting in a larger amount of residual ferrite in the weld melt zone (CARDOSO, 2012; GNANASEKARAN *et al.*, 2021; GENG *et al.* 2019; KUDDUS, 2018; CHENITI 2019; PERALTA 2013; LORA, 2006; ASADI *et al.*, 2020; GENG *et al.*, 2019). Another factor that significantly affects the cooling rate during welding is the thermal conductivity of the sample (RASHMI, MARUTHI *et al.*, 2018).

Austenitic stainless steels are not excellent thermal conductors and dissipate heat more slowly. However, the backing used to secure the specimens is considered to have excellent thermal conductivity which helps to dissipate the heat generated by the molten pool quickly (CARDOSO, 2012; KUMAR, 2021c).

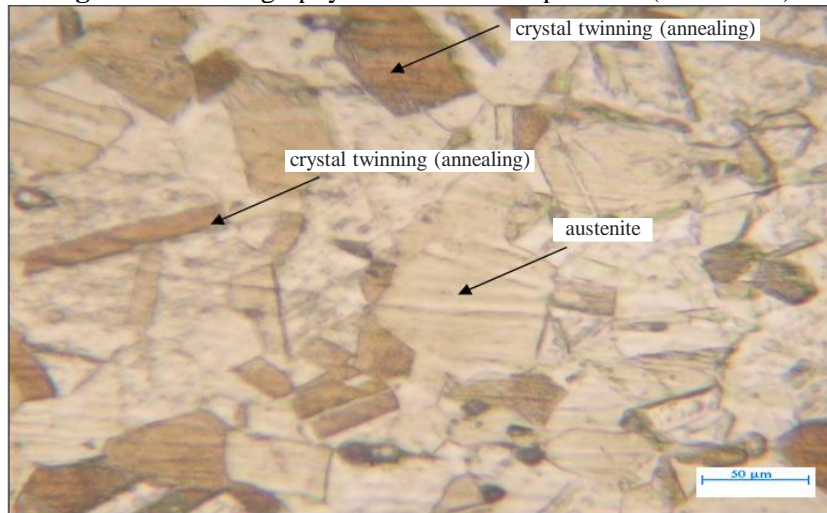
The sample, which was not welded, was microscoped and used as a standard to analyze the influence of heat input during welding. After metallographic examination, it was found that the standard cold rolled sample had a small hardening caused by deformation hardening during rolling.

From the metallography, shown in **Figure 5**, the presence of "parallel" grain contours, which are annealing twins (GNANASEKARAN *et al.*, 2021; CARDOSO, 2012; KUMAR *et al.*, 2019; KANT *et al.*, 2018) was detected.

The studied material was subjected to recrystallization annealing treatment, which results in progressive recovery of the plastically deformed microstructure, depending on the temperature increase (GNANASEKARAN *et al.*, 2021; CARDOSO, 2012; KUMAR *et al.*, 2021b; KANT *et al.*, 2021b; KANT *et al.*, 2021).

Austenitic stainless steels can be recrystallized at temperatures between 1000°C and 1100°C (CARDOSO, 2012). After maintaining this temperature for a certain time, followed by rapid cooling with air or water, the material acquires an essentially austenitic structure and with a smaller amount of other elements, mainly carbides (ITMAN *et al.*, 2014; KANT *et al.*, 2018). **Figures 6 to 10** show the metallographic analysis of the samples welded by the TIG process.

Figure 5: Metallography of the standard specimen (base metal)



Micrograph: Austenite with crystal twinning of annealing

Figure 6: Sample 01 - 0.94 kJ/cm (molten zone)

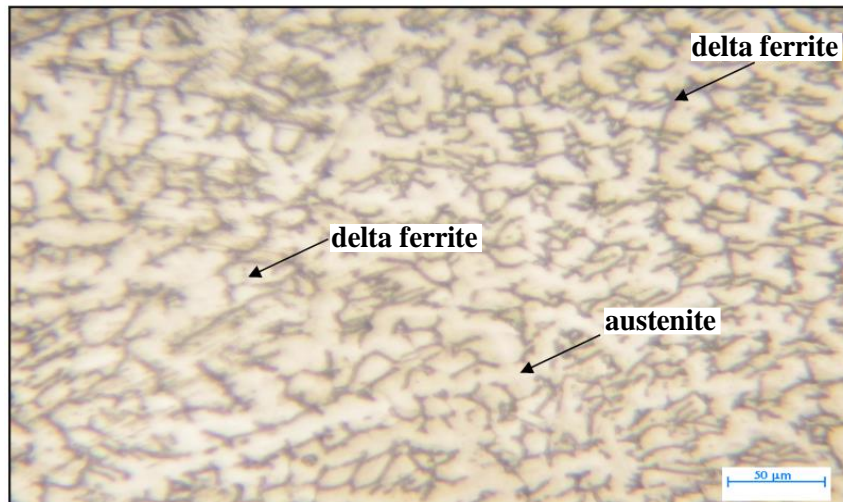


Figure 7: Sample 02 - 1.12 kJ/cm (molten zone)

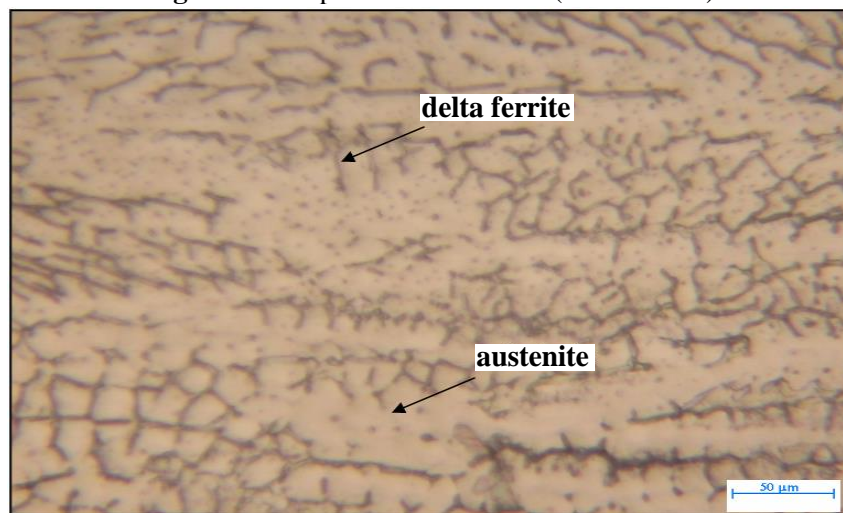


Figure 8: Sample 03 - 1.16 kJ/cm (molten zone)

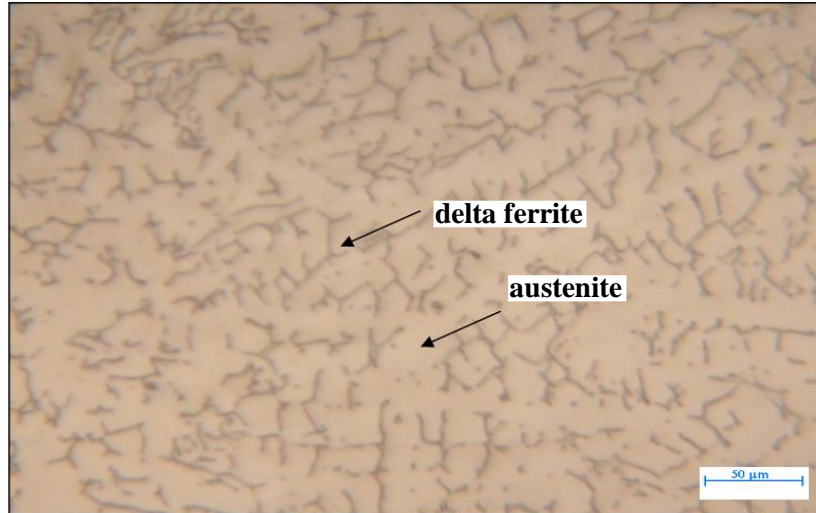


Figure 9: Sample 04 - 1.42kJ/cm (molten zone)

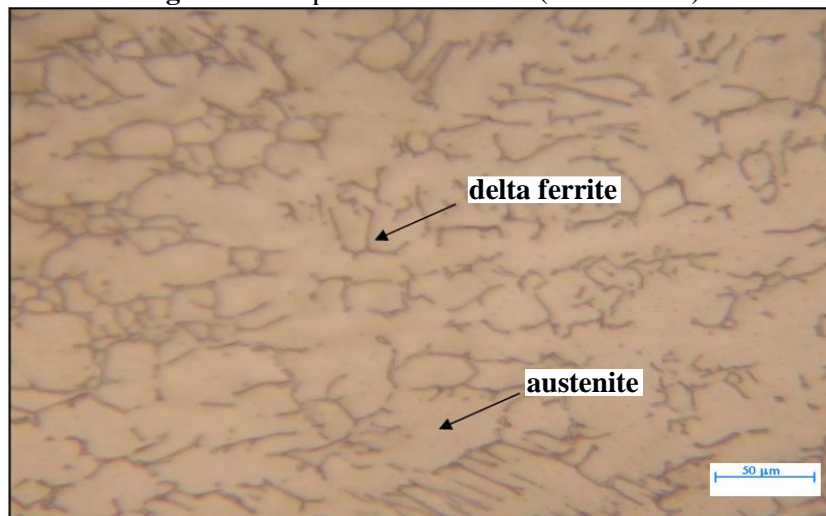
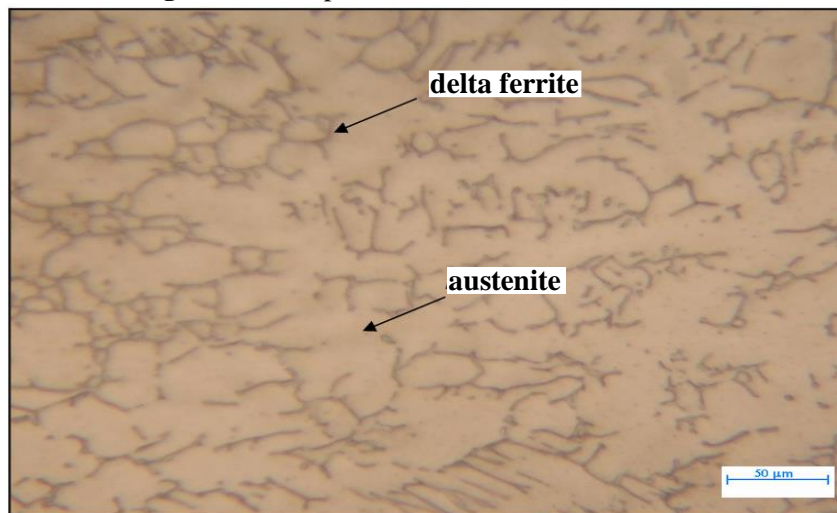


Figure 10: Sample 05 - 1.52 kJ/cm (molten zone)



Analysis of Figures 5 to 10 revealed a variation in the percentage of ferrite phase in the fusion zone of the samples. Using GSA software, this variation was also confirmed by quantifying the delta ferrite in the melt zone of the 5 samples.

Table 3 shows the amount of ferrite formed in each sample. It may be observed that the amount of ferrite retained varies with the intensity of the energy applied to the system.

It is also found that the higher the energy (E), the lower the ferrite content in the molten zone of stainless steel. This is related to the rate of cooling of the weld, which tends to decrease with increasing energy (E), making the thermal partitions more open.

The amount of ferrite estimated by the GSA software was generally considered satisfactory, as with the exception of sample 01, ferrite was present in the molten zone at levels between 5% and 10% in the other specimens, which has a beneficial effect to help dissolving low melting eutectic-forming elements, such as niobium, silicon, phosphorus and sulfur, by having a better ability to accommodate thermal stresses from cooling and by reducing the tendency to solidification cracks.

The ferrite content estimated by the software in Sample 01 is above 10%, which according to Peralta (2003) and

Kumar (2021a) is undesirable in the molten zone of the bead, especially at temperatures from 400 to 900°C, as the problem of "measuring" the ferrite content may occur, promoting the transformation of delta ferrite into brittle sigma phases, which negatively affects the mechanical properties and reduces toughness.

The retention of the steel in the temperature range between 400 and 900°C favours the precipitation of carbides ($M_{23}C_6$) along the contours and makes the steel susceptible to sensitization (ITMAN et al., 2014). The theory described by Arantes (2004) supports that the susceptibility to solidification cracking can be estimated by determining the residual delta ferrite content in the solid state.

The assessment was made by direct measurement of ferrite using GSA software, and the values of ferrite remaining in the molten zone between 5% and 10% are in the transition range of susceptibility to solidification cracking. The higher the residual ferrite content, the lower the susceptibility.

According to Peralta (2003), Arantes (2004) and Cheniti et al. (2019), there are other ways to estimate the susceptibility to solidification cracking besides the residual ferrite content, depending on the chemical composition and the primary microstructure of the solidification, which were not considered in this study.

Table 3: Amount of ferrite calculated by GSA software.

Sample	Welding energy (kJ/cm)	Delta ferrite average (%)	Standard deviation
S01	0.94	10.16	0.51
S02	1.12	7.85	1.43
S03	1.16	6.82	0.32
S04	1.42	6.34	0.32
S05	1.53	5.69	0.40

Table 4: Creq/Nieq and Primary Microstructure values.

Sample	Creq	Nieq	Creq/Nieq	Microstructure
01, 02, 03, 04, 05	17.88	9.30	1,92	Ferrite + Austenite

The results presented in **Table 4** were used to evaluate the chemical composition, because since the specimens were welded without filler metal, it was assumed that the chemical composition of the solder does not change significantly compared to the base material, but only in the coarse melt structure depending on the energy variation (E), as mentioned before.

The susceptibility is directly related to the C_{req}/N_{ieq} ratio used to determine the microstructure of the primary precipitates. Following Kejelin et al. (2019), C_{req} and N_{ieq} values were calculated using the parameters in **Figure 2**, **Table 1**, and **Equations (2) and (3)**.

$$C_{req} = \%Cr + \%Mo + 1.5\%Si + 0.5\%Nb \quad (2)$$

$$N_{ieq} = \%Ni + \%30\%C + 0.5\%Mn \quad (3)$$

The values in **Table 4** show that the C_{req}/N_{ieq} ratio was 1.92, which characterizes the primary precipitation of austenite and ferrite in the solidification phase and confirms that the C_{req}/N_{ieq} ratio at the given value is in the low susceptibility range of 1.5 to 2.0.

Comparing the obtained values with those from the literature, it is found that the weld of the specimens is in the transition range of susceptibility to solidification cracking.

5 CONCLUSIONS

From the quantification of ferrite by the GSA software, it appears that the increase in welding energy results in a decrease in the percentage of ferrite obtained for the values tested.

Therefore, it is considered that the cooling rate of the sample decreases and consequently there is more precipitation of austenite, decreasing the percentage of delta ferrite in the microstructure formed, thus affecting the results estimated by the GSA software.

In addition to the welding energy, other factors also affect the amount of ferrite found after solidification, such as the cooling rate, heat flux and chemical composition of the material under study (KUMAR, 2021a).

The weld beads of samples 01, 02, 03, 04 and 05 have ferrite contents below 10%, which classifies them as low susceptible to solidification cracking.

Ferrite in contents between 5 and 10% has a beneficial effect as it helps to dissolve elements forming eutectics with a low melting point and can better absorb the stresses generated during cooling.

The higher the heat flux for the same alloy, the lower the susceptibility to solidification cracking, since there is a higher cooling rate, which reduces the extent of transformation of ferrite into austenite, thus increasing the amount of ferrite remaining at room temperature.

ACKNOWLEDGMENTS

We would like to thank all those who contributed to the development of this research, including the Federal University of Espírito Santo (UFES), the Federal Institute of Espírito Santo (IFES) and ArcelorMittal Tubarão for providing equipment, laboratories and academic support.

REFERENCES

- Arantes, F. *Susceptibilidade ao trincamento do metal de solda depositado por diferentes eletrodos de aço inoxidável*. Dissertação (Mestrado) - Universidade Estadual de Campinas, Faculdade de Engenharia Mecânica, Campinas/SP, 2004
- Asadi, S. *et al.* Effects of Ni powder addition on microstructure and mechanical properties of NiTi to AISI 304 stainless steel archwire dissimilar laser welds.

Journal of Manufacturing Processes.
v.55, p.13-21, 2020
<https://doi.org/10.1016/j.jmapro.2020.03.041>

Avinash, S. *et al.* Multi-response optimization of pulse TIG welding process parameters of welds AISI 304 and Monel 400 using grey relational analysis.

Materials Today: Proceedings. vol.19, Part 2, p.296-301, 2019
<https://doi.org/10.1016/j.matpr.2019.07.211>

Balram, Y. *et al.* Effect of filler wires on weld strength of dissimilar pulse GTA Monel 400 and AISI 304 weldments. *Materials Today: Proceedings*. v.19, n.2, p.246-250, 2019a
<https://doi.org/10.1016/j.matpr.2019.06.759>

Balram, Y. *et al.* Residual stress analysis of dissimilar tungsten inert gas weldments of AISI 304 and Monel 400 by numerical simulation and experimentation. *Materials Today: Proceedings*. v.19, n.2, p.478-483, 2019b
<https://doi.org/10.1016/j.matpr.2019.07.639>

Cardoso, Wandercleiton. *Efeitos do nióbio na microestrutura e resistência à corrosão do aço inoxidável austeno-ferrítico SEW 410 NR. 1.4517*. Dissertação (Mestrado em Engenharia Metalúrgica e de Materiais) - Departamento de Engenharia, Instituto Federal de Educação, Ciência e Tecnologia do Espírito Santo (IFES), Vitória/ES, 2012
<https://doi.org/10.29327/4227903>

Casalino, G. *et al.* Study on the fiber laser/TIG weldability of AISI 304 and AISI 410 dissimilar weld. *Journal of Manufacturing Processes*. v.35, p.216-225, 2018
<https://doi.org/10.1016/j.jmapro.2018.08.005>

Cheniti B. *et al.* Microstructure and mechanical behavior of dissimilar AISI 304L/WC-Co cermet rotary friction welds. *Materials Science and Engineering*. v.758, p.36-46, 2019
<https://doi.org/10.1016/j.msea.2019.04.081>

Corrêa Jr, Joani Genelhu. *Efeito do processamento termomecânico na resistência à fadiga de um aço IF*. Dissertação (Mestrado), Universidade Federal de Ouro Preto, Departamento de Engenharia de Materiais, Ouro Preto/MG, 2012

Geng, Y. *et al.* Effects of the laser parameters on the mechanical properties and microstructure of weld joint in dissimilar pulsed laser welding of AISI 304 and AISI 420. *Infrared Physics & Technology*. v.103, 2019
<https://doi.org/10.1016/j.infrared.2019.103081>

Giraldo, Claudia Patricia Serna. *Precipitação de fases intermetálicas na zona afetada pelo calor de baixa temperatura (ZACTB) na soldagem multipasses de aços inoxidáveis duplex*. Dissertação (Mestrado) – Universidade de São Paulo, Departamento de Eng. Metalúrgica, Escola Politécnica, São Paulo/SP, 2011

Gnanasekaran, S. *et al.* Effect of laser power on microstructure and tensile properties of pulsed Nd:YAG laser beam welded AISI 301 austenitic stainless steel joints. *Materials Today: Proceedings*. v.37, n.2, p.934-939, 2021
<https://doi.org/10.1016/j.matpr.2020.06.145>

Han, L. *et al.* Local dry underwater welding of 304 stainless steel based on a microdrain cover. *Journal of Materials Processing Technology*. v.268, p.47-53, 2019
<https://doi.org/10.1016/j.jmatprotec.2018.12.029>

Itman, Andre; Cardoso, Wandercleiton; Gontijo, Leonardo Cabral; Vilarim da Silva, Rosana; Casteletti, Luiz Carlos. Austenitic-ferritic stainless steel containing niobium. *REM: Revista Escola de Minas*. v.66, n.4, p.467-471, 2013
<https://doi.org/10.1590/S0370-44672013000400010>

Itman, Andre; Cardoso, Wanderleiton; Vilarim da Silva, Rosana; Casteletti, Luiz Carlos. Effect of niobium in the phase transformation and corrosion resistance of one austenitic-ferritic stainless steel. *Materials Research*. v.17, n.4, p.801-806, 2014
<https://doi.org/10.1590/1516-1439.190113>

Jijin, X. *et al.* Comparison of residual stress induced by TIG and LBW in girth weld of AISI 304 stainless steel pipes, *Journal of Materials Processing Technology*. v.248, p.178-184, 2017
<https://doi.org/10.1016/j.jmatprotec.2017.05.014>

Kant, R. *et al.* Fabrication and Characterization of Weldments AISI 304 and AISI 316 Used in Industrial Applications. *Materials Today: Proceedings*. v.5, n.9 p.18475-18481, 2018
<https://doi.org/10.1016/j.matpr.2018.06.189>

Kejelin, Norton Zanette; Buschinelli, Augusto José de Almeida, Bohórquez, Augusto José de Almeida. Dissimilar Metal Welding of X-60 Steel with Inconel 625. *Labsolda UFSC*. vol.1, p.01-10, 2019

Kripalani, K.; Jain, P. Experimental investigations of various joinery methods on repaired AISI 304 A plate with Nitinol wire. *Materials Today: Proceedings*. v.37, n.2, p.2093-2103, 2021
<https://doi.org/10.1016/j.matpr.2020.07.522>

Kuddus, Abdul Irshad *et al.* Microstructural, mechanical and corrosion behaviour of dissimilar welding of Cr-Mn ASS and AISI 304 ASS by using 316L electrode. *Materials Today: Proceedings*. v.5, n.2, p.8307-8313, 2018
<https://doi.org/10.1016/j.matpr.2017.11.522>

Kumar, Rohit *et al.* Effect of Activated Flux on TIG Welding of 304 Austenitic Stainless Steel. *Materials Today: Proceedings*. v.18, n.7, p.4792-4798, 2019
<https://doi.org/10.1016/j.matpr.2019.07.467>

Kumar, P. *et al.* Study of phase changes induced by gamma irradiation in welded stainless steel alloys 304 and 316. *Materials Today: Proceedings*, 2021a
<https://doi.org/10.1016/j.matpr.2021.01.815>

Kumar, Rohit. Comparative study of TIG and MIG welding for Bi-metallic weld of AISI 304 and monel 400. *Materials Today: Proceedings*. v.37, n.2, p.3501-3504, 2021b
<https://doi.org/10.1016/j.matpr.2020.09.395>

Kumar, Rohit. Study of TIG welding on bi-metal weld AISI 304 and Monel 400. *Materials Today: Proceedings*. v.37, n.2, p.3512-3515, 2021c
<https://doi.org/10.1016/j.matpr.2020.09.398>

Lora, Marcio Cunha. *Influência da energia de soldagem sobre a microestrutura da zona Fundida do aço inoxidável duplex AISI 2205*. Monografia (Engenharia) – Departamento de Engenharia Mecânica, Universidade Federal do Espírito Santo, Vitória/ES, 2006

Maruthi, G.; Purushotham, N.; Rashmi, R. Low Temperature Embrittlement studies on Stainless Steel 304 LN TIG Welds. *Materials Today: Proceedings*. v.5, n.1, p.2891-2900, 2018
<https://doi.org/10.1016/j.matpr.2018.01.083>

Mishra, D.; Dakkili, M. Gas tungsten and shielded metal arc welding of stainless steel 310 and 304 grades over single and double ‘V’ butt joints. *Materials Today: Proceedings*. v.27, n.2, p.772-776, 2020
<https://doi.org/10.1016/j.matpr.2019.12.189>

Moharana, B. R. *et al.* An experimental study on joining of AISI 304 SS to Cu by Nd-YAG laser welding process. *Materials Today: Proceedings*. v.33, n.8, p.5262-5268, 2020
<https://doi.org/10.1016/j.matpr.2020.02.953>

Pankaj, P. *et al.* Experimental investigation on CO₂ laser butt welding of AISI 304 stainless steel and mild steel thin sheets.

Optics & Laser Technology. v.119, 2019
<https://doi.org/10.1016/j.optlastec.2019.105633>

Patel, N. *et al.* Review on the use of activated flux in arc and beam welding processes. **Materials Today: Proceedings.** v.43, n.2, p.916-920, 2021
<https://doi.org/10.1016/j.matpr.2020.07.218>

Peralta, Joao Lobo. *Análise do defeito da deformação na formação da microestrutura e na rejeição de soluto durante a solidificação de placas finas.* Tese (Doutorado) - Universidade Estadual de Campinas, Faculdade de Eng. Mecânica, Campinas/SP, 2003

Ramakrishnan, A. *et al.* Experimental investigation on mechanical properties of TIG welded dissimilar AISI 304 and AISI 316 stainless steel using 308 filler rod. **Materials Today: Proceedings,** 2021
<https://doi.org/10.1016/j.matpr.2021.03.502>

Saroj, S.; Sahoo, C.; Masanta, M. Microstructure and mechanical performance of TiC-Inconel825 composite coating deposited on AISI 304 steel by TIG cladding process. **Journal of Materials Processing Technology,** v.249, p.490-501, 2017
<https://doi.org/10.1016/j.jmatprotec.2017.06.042>

Saroj, S.; Sahu, A.; Masanta, M. Geometrical assessment and mechanical characterization of single-line Inconel 825 layer fabricated on AISI 304 steel by TIG cladding method. **Surfaces and Interfaces.** v.20, 2020
<https://doi.org/10.1016/j.surfin.2020.100631>

Shanm, G. *et al.* Optimization of Process Parameters in TIG Welded Joints of AISI 304L -Austenitic Stainless Steel using Taguchi's Experimental Design Method. **Materials Today: Proceedings.** v.16, n.2, p.1188-1195, 2019
<https://doi.org/10.1016/j.matpr.2019.05.213>

Shuang, L. *et al.* Keyhole process in K-TIG welding on 4mm thick 304 stainless steel. **Journal of Materials Processing Technology.** v.243, p.217-228, 2017
<https://doi.org/10.1016/j.jmatprotec.2016.12.027>

Soltani, H.; Tayebi, M. Comparative study of AISI 304L to AISI 316L stainless steels joints by TIG and Nd:YAG laser welding. **Journal of Alloys and Compounds.** v.767, p.112-121, 2018
<https://doi.org/10.1016/j.jallcom.2018.06.302>

Sun, J. *et al.* Fiber laser welding of thick AISI 304 plate in a horizontal (2G) butt joint configuration. **Materials & Design.** v.118, p.53-65, 2017
<https://doi.org/10.1016/j.matdes.2017.01.015>

Tang, X. *et al.* Tribological and cavitation erosion behaviors of nickel-based and iron-based coatings deposited on AISI 304 stainless steel by cold metal transfer. **Journal of Materials Research and Technology.** v.9, n.3, p.6665-6681, 2020
<https://doi.org/10.1016/j.jmrt.2020.04.064>

Xiaogang, L. *et al.* Failure mechanism transition of hydrogen embrittlement in AISI 304 K-TIG weld metal under tensile loading. **Corrosion Science.** v.130, p.241-251, 2018
<https://doi.org/10.1016/j.corsci.2017.10.032>

Zumelzu, E.; Cabezas, C. Study on welding such dissimilar materials as AISI 304 stainless steel and DHP copper in a sea-water environment. Influence of weld metals on corrosion. **Journal of Materials Processing Technology.** v.57, n.3, p.249-252, 2021 [https://doi.org/10.1016/0924-0136\(95\)02073-X](https://doi.org/10.1016/0924-0136(95)02073-X)